EARLY CAREER SCHOLARS IN MATERIALS SCIENCE 2022

Synthesis and behavior of bulk iron nitride soft magnets via high-pressure spark plasma sintering

Todd C. Monson[1,a)] , **Baolong Zheng**[2], **Robert E. Delaney**[1], **Charles J. Pearce**[1], **Yizhang Zhou**[2], **Stanley Atcitty**[1], **Enrique Lavernia**[2]

[1] *Sandia National Laboratories, Albuquerque, NM 87185, USA*
[2] *University of California, Irvine, CA 92697, USA*
a) Address all correspondence to this author. e-mail: tmonson@sandia.gov

Received: 25 May 2021; accepted: 2 September 2021; published online: 1 November 2021

In this study, dense bulk iron nitrides (Fe_xN) were synthesized for the first time ever using spark plasma sintering (SPS) of Fe_xN powders. The Fe_4N phase of iron nitride in particular has significant potential to serve as a new soft magnetic material in both transformer and inductor cores and electrical machines. The density of SPSed Fe_xN increased with SPS temperature and pressure. The microstructure of the consolidated bulk Fe_xN was characterized with X-ray diffraction (XRD), scanning electron microscopy (SEM), transmission electron microscopy (TEM), and superconducting quantum interference device (SQUID) magnetometry. XRD revealed a primary phase of Fe_4N with secondary phases of Fe_3N and metallic iron. Finite element analysis (FEA) was also applied to investigate and explain localized heating and temperature distribution during SPS. The effects of processing on interface bonding formation and phase evolution were investigated and discussed in detail to provide insight into fundamental phenomena and microstructural evolution in SPSed Fe_xN.

Todd C. Monson is a Principal Member of the Technical Staff at Sandia National Laboratories, where he has worked since 2005. Todd earned both a Ph.D. (2012) and M.A. (2001) in physics from the University of Texas at Austin. Prior to coming to Sandia, Todd served as a physicist in the U.S. Air Force for over seven years, working at both the Air Force Research Laboratory's Munitions Directorate and serving as an assistant professor of physics at the U.S. Air Force Academy. Todd received his commission in the U.S. Air Force after graduating with a B.S. in physics from the U.S. Naval Academy in May of 1997. Todd's research interests include the synthesis and characterization of ferromagnetic and ferroelectric materials in both bulk and composite form. He seeks greater understanding of ferroic behavior at all length scales from ranging from Ångstrom to macroscale. In the field of magnetics, Todd's research has primarily focused on the synthesis of new soft magnetic materials to enable increased power density and energy efficiency in inductors, transformers, and electrical machines.

Introduction

New, high-saturation magnetization (M_s) and low-loss soft magnetic materials will be vital for the next generation of power conversion electronics and electrical machines [1]. Since iron nitrides (Fe_xN, $x = 2–4$) are comprised entirely of low-cost abundant elements and many phases of the iron nitride system offer the promise of better magnetic properties, this class of materials beckons further investigation [2, 3].

Fe_xN has been studied for decades due to both its ability to improve surface hardness and wear resistance of components [4] and impressive magnetic properties [5–9]. According to experimental results [2, 10, 11] from thin films and theoretical calculations [2], several phases of iron nitride would have magnetic moments well in excess of current state of the art soft magnetic materials. Therefore, Fe_xN would be ideally suited for use in many applications, such as both transformer and inductor

cores and in electrical machines. To date, Fe$_x$N has primarily been fabricated as thin films, powder, or inclusions in other materials [11, 12]. Bulk Fe$_x$N was rarely fabricated because a relatively high sintering temperature is required using conventional powder sintering processes. Fe$_x$N is semi-metallic and generally thermally metastable. The decomposition of Fe$_x$N into Fe and N$_2$ upon heating to 863 K was previously noted [13, 14]. Therefore, dense bulk Fe$_x$N is challenging to synthesize.

Spark plasma sintering (SPS), a low-temperature field-assisted sintering technique (FAST), has been studied as an attractive consolidation technique for powder. SPS uses pulsed current and pressure to achieve lower sintering temperatures, fast heating rates, and brief consolidation cycles [15–17]. In view of the above facts, we have investigated the synthesis and magnetic behavior of dense bulk Fe$_x$N from Fe$_x$N powders using SPS, which enables the direct consolidation and shaping of Fe$_x$N transformer and inductor cores from raw starting materials in a matter of minutes, without the decomposition of Fe$_x$N that would occur using conventional sintering techniques [13]. Microstructural evaluation of consolidated samples using SPS

was then evaluated using X-ray diffraction (XRD), scanning electron microscopy (SEM), and transmission electron microscopy (TEM). Their magnetic properties were also measured and evaluated using magnetometry. COMSOL FEA software was also applied to investigate and explain the localized heating and temperature distribution during SPS of Fe$_x$N powder. The underlying mechanisms of interface bonding and formation, thermal stability, and phase transition are also discussed in an effort to elucidate fundamental phenomena in SPSed Fe$_x$N.

Results

Microstructure of SPSed Fe$_x$N

The typical microstructure corresponding to SPSed Fe$_x$N (at 823 K and 350 MPa) is shown in Fig. 1a. At low magnification in the polished sections, uniform contrast is observed without secondary phases being evident. Almost full densification (up to 99% of the theoretical density of Fe$_4$N), without visible porosity, was achieved in the SPSed Fe$_x$N samples. The interfaces between particles are not evident, suggesting that the
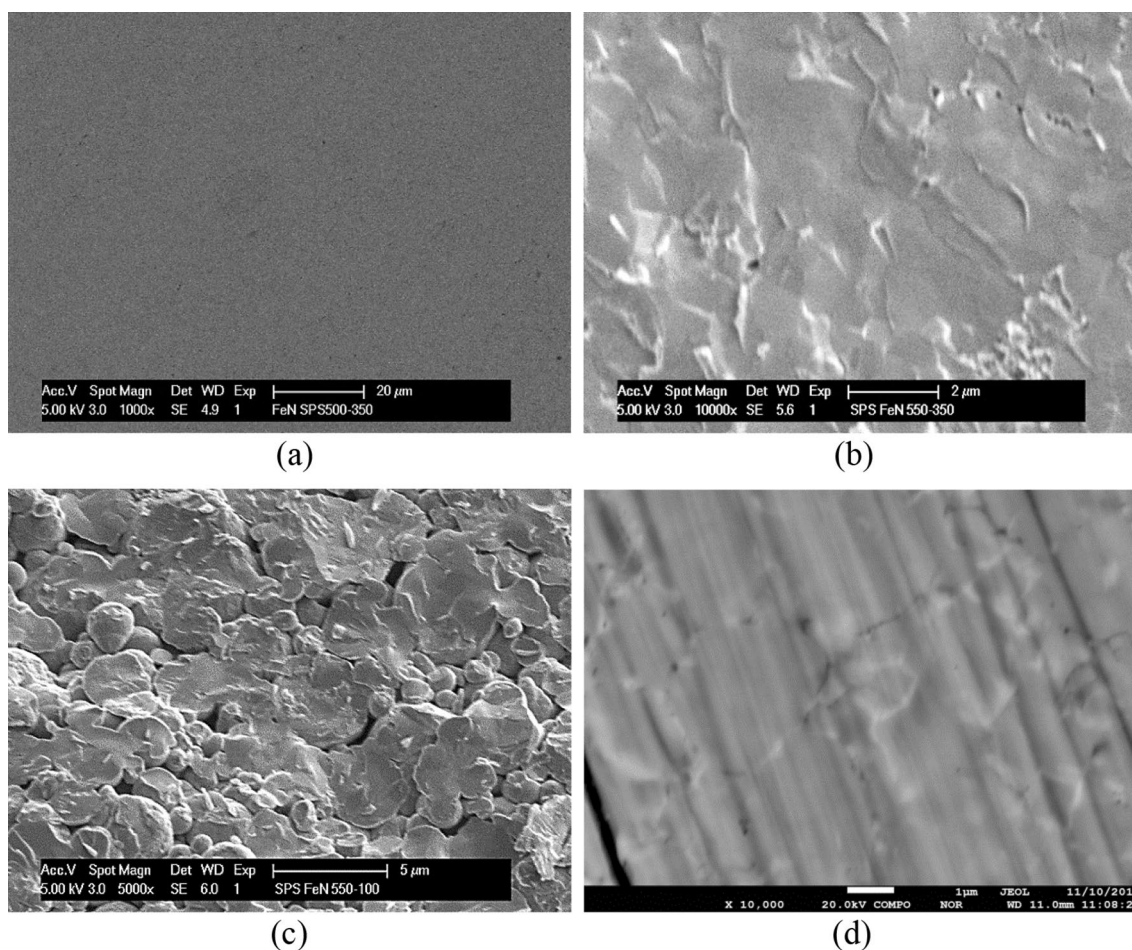

Figure 1: SEM micrograph and fractograph of SPSed Fe$_x$N samples with different pressures (a), (b) 823 K, 350 MPa, (c) 823 K, 100 MPa, and (d) the surface of a toroid sintered at 823 K, 100 MPa.

interface bonding between particles was enhanced compared with samples SPSed at a lower pressure of 100 MPa. A small volume fraction (approximately 0.8 vol% measured from SEM imaging) of pores was observed in the microstructure of samples SPSed at 823 K and 350 MPa, as shown in Fig. 1b. It was also observed that the density of SPSed Fe_xN samples clearly increased with SPS pressure. The fracture surface corresponding to this SPSed Fe_xN material, shown in Fig. 1b and c, reveals transparticle fracture features, which suggests strong particle–particle bonding formation and effective load transfer. It is interesting to observe that there is a variation of contrast around the particles' boundaries, as shown in Fig. 1d. A variation in composition was observed in SPSed Fe_xN between the particles' boundaries and centers. Traces collected using wavelength dispersive spectroscopy (WDS) showed that the stoichiometry in the center of each grain is close to Fe_4N (81.3 at.% Fe), while the iron content at the grain boundaries (GBs) is about 3 atomic percent richer (84.2 at.% Fe). The slightly higher concentration of Fe at the grain boundaries in the WDS data is consistent with the lighter grain boundaries seen in the backscattered electron (BSE) SEM image (refer to Figure S1). Table S1 in the supplementary information summarizes the WDS data from the surface of a sintered toroid.

Figure 2 shows the XRD patterns corresponding to Fe_xN SPSed at 773 K, 798 K, and 823 K with pressures ranging from 200 to 500 MPa. XRD analysis indicates that SPSed Fe_xN contains primarily two crystalline phases, Fe_4N and Fe_3N. One Fe_xN sample sintered at 823 K and 350 MPa shows a peak around a 2Θ value of 26°, likely due to decomposition of Fe_xN into iron metal. This decomposition may be occurring due to localized higher temperatures during sintering and the increased pressure used during the consolidation of this sample. Other SPSed samples did not exhibit the same peak.

The microstructure and interface characteristics of SPSed Fe_xN were further investigated by TEM analysis. A typical bright field TEM micrograph of the microstructure of SPSed Fe_xN at 823 K and 200 MPa is shown in Fig. 3. The Fe_xN particles once again appear well consolidated with very little porosity. The voids between particles have almost entirely disappeared. Twins were also observed in some SPSed Fe_xN grains. Twin boundaries (TBs) can greatly improve mechanical properties [18], such as strength and ductility. The grain size of SPSed Fe_xN ranged from 200 nm to 1 μm.

Properties of SPSed Fe_xN

To investigate the thermal stability of Fe_xN, differential scanning calorimetry (DSC) was used, as shown in Fig. 4. During heating, there is an exothermic event beginning at 873 K, corresponding to the decomposition of Fe_xN. Therefore, sintering temperatures must be kept below this temperature to avoid simultaneous decomposition during consolidation.

The densities of Fe_xN consolidated using different sintering temperatures and pressures are shown in Fig. 5. As expected, density increases with increasing SPS temperature and pressure. The highest density of 7.08 g/cm³ was achieved in a sample SPSed at 773 K and 500 MPa. This equates to 99% of the theoretical density of Fe_4N (7.179 g/cm³).

The density of Fe_xN samples produced with MM powder was also measured. AR Fe_xN powder was mechanical milled using a high-energy ball miller (SPEX 8000D) for 4 h in argon
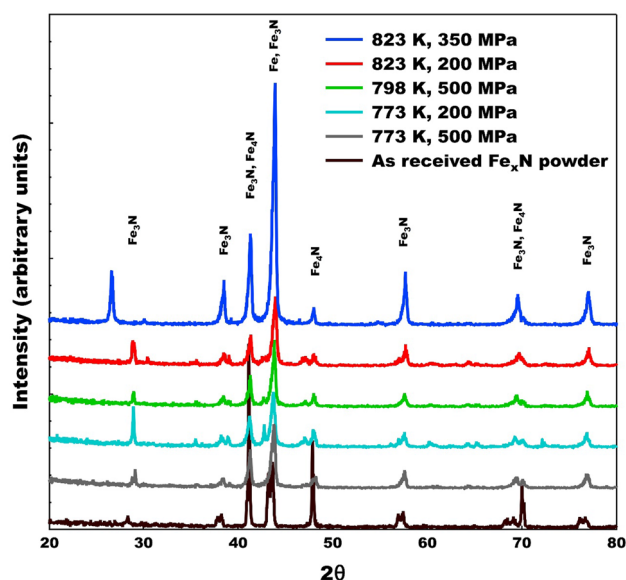

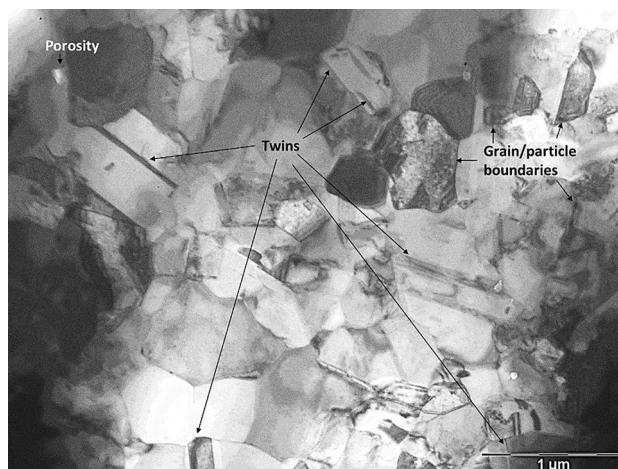**Figure 2:** XRD patterns of bulk Fe_xN samples SPSed with different conditions.

Figure 3: TEM bright field micrograph of SPSed Fe$_x$N at 823 K and 200 MPa.
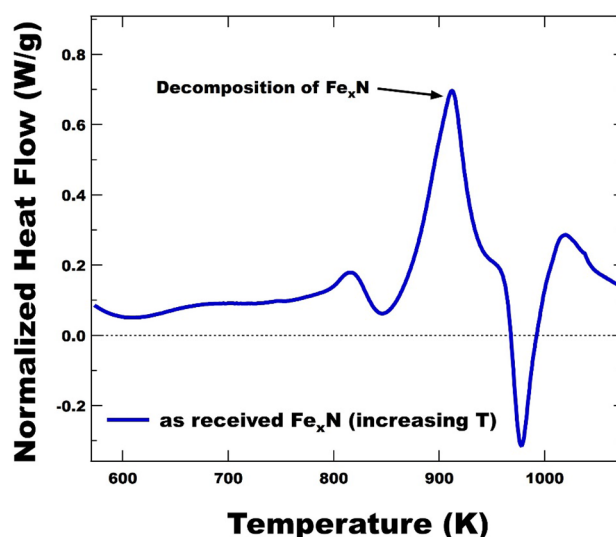

Figure 4: DSC pattern of bulk Fe$_x$N sample SPSed at 823 K and 200 MPa. Endothermic reactions are represented by positive heat flow (*y*-axis).

atmosphere at room temperature. The ball to AR Fe$_x$N powder weight ratio used in our experiments was 5:1. The density of samples produced using milled Fe$_x$N powder is significantly higher than those produced with AR Fe$_x$N powder under the same SPS processing conditions. Increased density is most likely due to higher packing density and greater diffusion during sintering as a result of finer particle sizes [19]. Additionally, there is a higher degree of variation in the density of samples produced with AR powder when compared with those produced with milled Fe$_x$N powder.

Magnetic properties of the SPSed Fe$_x$N samples were also investigated. Figure 6 shows the magnetic hysteresis (*M* vs. *H*) curves of the SPSed Fe$_x$N with as-received FexN powder. The saturation magnetization (M_s), coercivity (H_c), and relative permeability (μ_r) of the samples vary only slightly with SPS

temperature and pressure. Fe$_x$N sintered at 823 K and 200 MPa achieved a M_s of 188 A·m^2/kg, a H_c of 9.20×10^2 A/m, and a μ_r of 6.84. The measured value of M_s is less than the theoretical value of 209 A·m^2/kg [3], which is primarily due to presence of the secondary Fe$_3$N phase. The soft magnetic properties of SPSed FexN could be further improved by improving phase purity of the raw materials, refining grain size of the raw materials, and optimizing SPS-processing conditions to persevere both phase purity and a fine grain size.

Discussion

Consolidation of nitrides generally requires both high temperatures and pressures. However, the relatively low thermal stability of Fe$_x$N (recall decomposition begins at 873 K) limits the use of
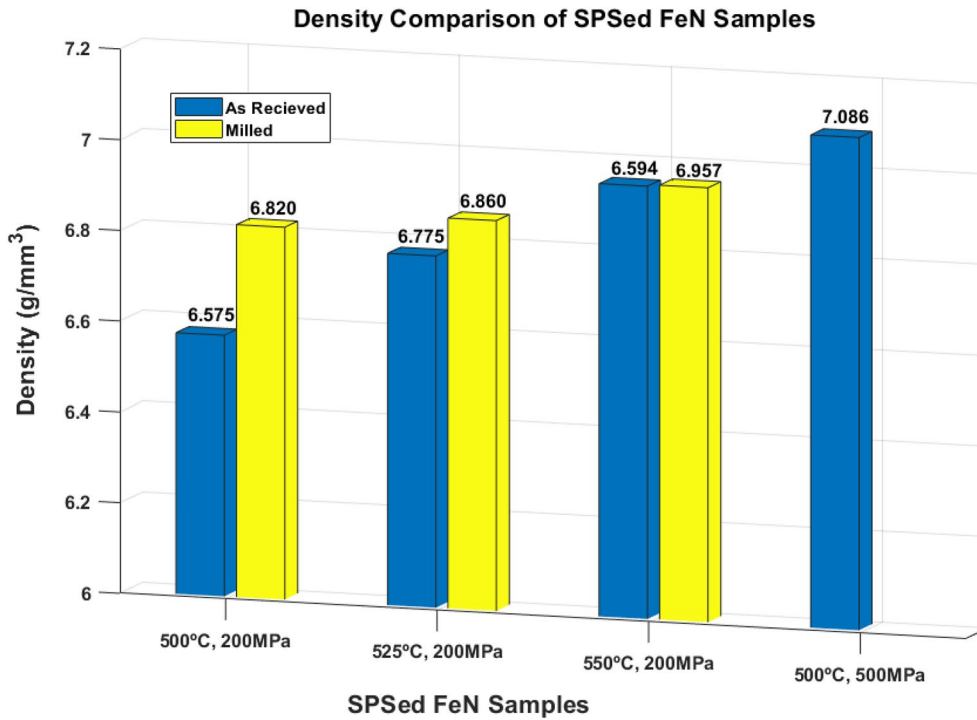
Figure 5: Density of SPSed Fe$_x$N samples with AR and milled Fe$_x$N powder. As a reference, the theoretical density of Fe$_4$N is 7.179 g/cm^3.
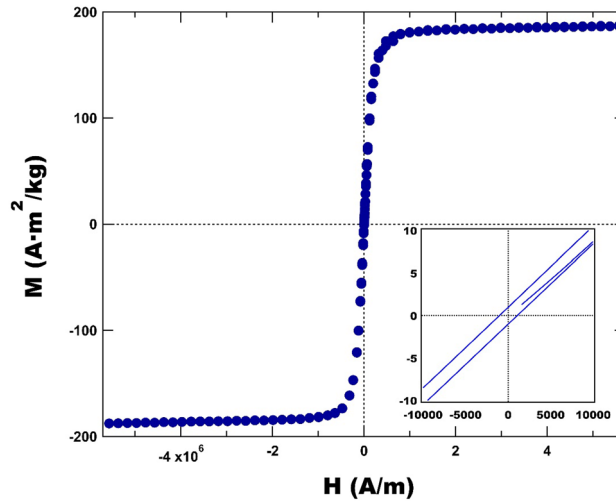

Figure 6: Field dependent magnetic response of SPS consolidated Fe$_x$N.

higher temperature for consolidation. Therefore, SPS is the most suitable approach for consolidating dense, bulk Fe$_x$N.

The SPS process represents a multiple-field problem in which the electric, thermal, and displacement (i.e., shrinkage) fields are coupled via a material response. This problem is strongly nonlinear since the fields interact and affect the properties of SPSed materials. The consolidation of Fe$_x$N with SPS is related to the deformation behavior of each particle, which also depends on internal defects (i.e., grain boundaries

(GBs), dislocations, twins, vacancies, etc.,), as well as the local pressure and temperature. In particular, spatial variations in the thermal and stress fields are likely conditions that can promote interface bonding and formation. During SPS, a pulsed current passes though both die and powder (according to its electrical conductivity), which will promote thermal energy and mass transfer. The thermal energy generated in the graphite die from Joule heating is transferred to the powder via conduction and limited radiation. The heat transfer

in sintered particles can be expressed in the thermal energy equation as follows [20]:

$$\frac{1}{r^2}\frac{\partial}{\partial r}\left(kr^2\frac{\partial T}{\partial r}\right) + \frac{1}{r^2\sin^2\theta}\frac{\partial}{\partial \varphi}\left(k\frac{\partial T}{\partial \varphi}\right) + \frac{1}{r^2\sin\theta}\frac{\partial}{\partial \theta}\left(k\sin\theta\frac{\partial T}{\partial \theta}\right) + \dot{q} = \rho c_p\frac{\partial T}{\partial t} \tag{1}$$

where ρ is density, c_p is specific heat, and q is energy rate generated per unit volume for conduction analysis with spherical coordinates (r, Φ, θ). In the case of micron-sized particles, the internal temperature is equilibrated within several milliseconds. However, during SPS processing, the continuity of the electric field is disrupted by the presence of multiple interfaces. A local increase in temperature from electrical Joule heating can be calculated using Joule's law, as follows:

$$T = I^2 \cdot R \cdot t/m \cdot c_p \tag{2}$$

where I is the electric current, R is electrical resistance, t is time, m is mass, and c_p is the specific heat of the SPSed materials. Local increases in temperature will occur from the combination of a small contact area and a high local current density, as shown in Fig. 7, a FEA simulation of the early stage of sintering. Contact areas contain higher current and heat flux, and flat contact areas contain twice as much current/heat flux than in slanted contact areas. It has also been proposed that a spark discharge may occur at inter-particle regions [15], leading to localized partial melting and perhaps even to the formation of a metallic vapor [21] for some alloys as a result of elevated localized temperatures. Under the influence of the pressure, thermal, and electromagnetic fields, constricted geometries or "necks" are formed around the contact area between particles by localized heating and localized high stress, which can result in surface activation. These necks gradually develop and deformation progresses during sintering, resulting in densification. Meanwhile, grain growth or decomposition is possible at the contact
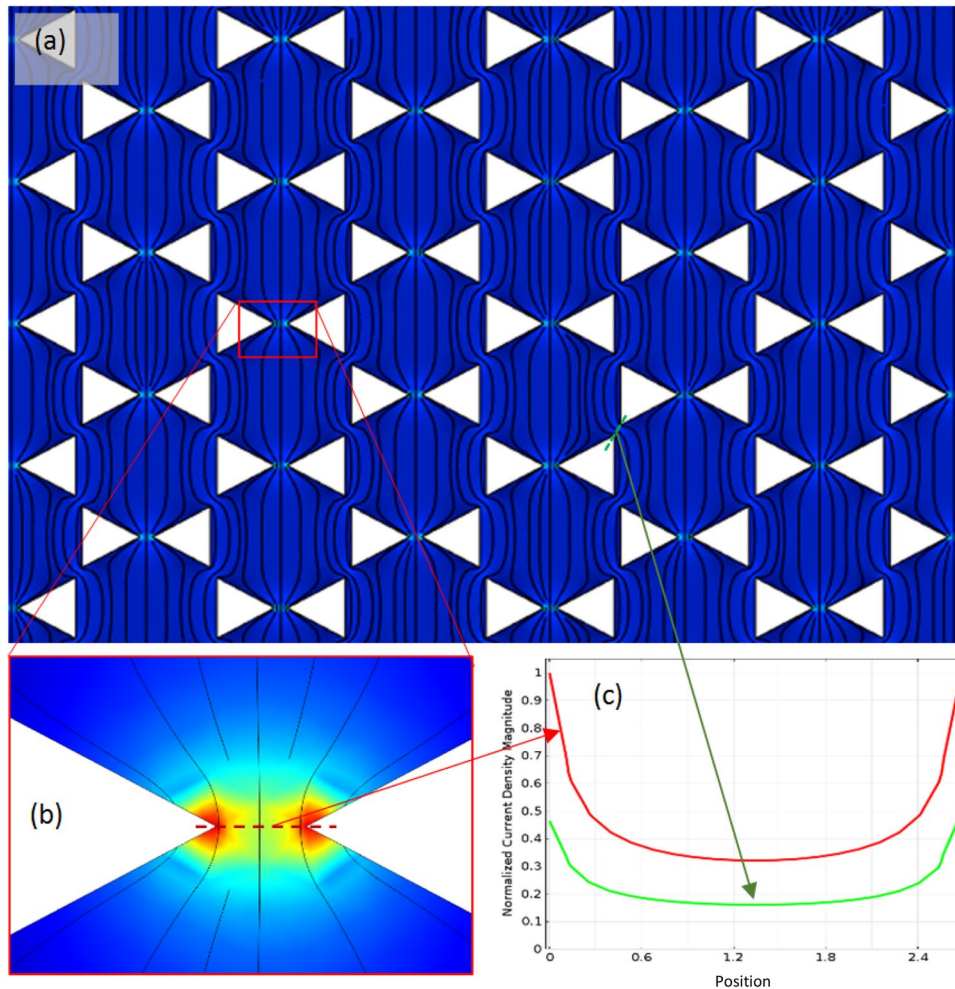

Figure 7: FEA simulation results of current/heat flux concentrations on the outer portions of the contact areas.

area between particles due to the activation of localized higher temperature and stress [22, 23]. As shown both in the WDS data discussed previously and in the BSE SEM image in Fig. 1d (see also Figure S1), Fe_xN partially decomposed at the particle boundary, resulting in a decreased amount of N because the localized temperature in the particle boundary was higher than the decomposition temperature of Fe_xN, 873 K.

As many twins are present in SPSed Fe_xN, as shown in Fig. 3, the strength and ductility of SPSed Fe_xN can be improved as it has been revealed that twin boundaries (TBs) can greatly improve the strength and ductility of brittle materials. Dislocation accumulation in TBs for brittle materials, such as carbides and nitrides [1], creates strength and ductility enhancement [18, 24]. Thus, this represents a strategy by which SPSed Fe_xN might gain some plasticity. The formation of twins can thermodynamically decrease the total interfacial energy, because the excess energy for coherent TBs is much smaller than that for conventional high-angle GBs. It was reported that twins prefer to nucleate at GBs to reduce the sum of the interfacial energies (including GBs and TBs) [18] by means of the twinning-induced orientation change.

The milled Fe_xN powders were found to exhibit a marked improvement in density after SPS processing relative to AR spherical Fe_xN powders. This can be attributed to the obvious differences in particle morphology and increase in surface area per unit volume. The AR Fe_xN powders have a spherical shape with a relatively smooth surface whereas the milled powders have an irregular morphology and rough surface in addition to a smaller average size. Surface area per unit volume and curvature both increase with decreasing particle size, resulting in higher energy per unit volume, which enhances diffusion and thus sintering kinetics [17, 25]. Neck growth during sintering, for example, increases with decreasing particle size. Another important influence of particle size on sintering is related to a temperature reduction with particle size, which can be expressed by [25]:

$$T_2 = \cfrac{1}{\frac{1}{T_1} - \frac{KM}{Q} \ln \frac{D_2}{D_1}} \qquad (3)$$

where T_1 and T_2 are the sintering temperatures for a change in particle size of D_1 and D_2, respectively, assuming the sintering time is constant. M is a constant, Q is the sintering activation energy, and K is the Boltzmann's constant. If $D_2 < D_1$, $T_2 < T_1$, and a lower sintering temperature can be used.

It is anticipated that the soft magnetic properties of nanostructured Fe_xN materials can benefit from grain refinement [26]. Moreover, both a reduction in electrical conductivity and an increase in thermal conductivity are also requirements for the application of Fe_xN as soft magnetic materials. Both the electrical and thermal conductivity of a material are related to the scattering of electrons or photons [27]. The

electrical resistivity increases as a result of electron scattering by imperfections, such as grain boundaries (GBs), impurities, dislocations and vacancies. On the other hand, thermal conductivity mainly depends on phonon scattering by GBs and the presence "insulating" phases (such as porosity). As a rule of thumb, decreasing the electrical conductivity while simultaneously increasing thermal conductivity is a challenge for most of materials. Thermal and electrical conductivity measurements of Fe_4N will be forthcoming in future work as improvements to phase purity in SPSed samples are realized.

Nanostructured Fe_xN powder can be formed through ball milling of as-received Fe_xN powder. Recall, GBs in crystal materials behave as obstacles for electron and thermal transmission. Nanocrystals have large surface-to-volume ratios, so the electrical conductivity of nanocrystalline materials is lower than that of the corresponding coarse-grained materials. In addition, it is known that the soft magnetic properties (increased μ and reduced H_c) can be further improved by reduction in grain size [28].

In addition to grain refinement into the nanocrystalline range and the accompanying high volume fraction of GBs induced by ball milling, nanostructures store a large excess of energy in non-equilibrium defects, such as dislocations, and vacancies, which constitute effective obstacles for electron transport, decreasing the electrical conductivity. Therefore, the electrical conductivity of bulk Fe_xN can be decreased by developing nanocrystalline structures and defects in Fe_xN using high-energy ball milling. We do have to consider that the grain refinement may also lead to a reduction in the thermal conductivity. However, the magnitude of change, from grain refinement, in electrical conductivity and the thermal conductivity of nanocrystalline Fe_xN may vary, and will require furthermore investigation. Once again, improvements in the final phase purity of sintered Fe_4N will be required before undertaking this study.

The thermal conductivity of SPSed Fe_xN can be enhanced by increasing the density of consolidated Fe_xN by through the use of high pressure (up to 500 MPa). The thermal conductivity of materials decreases with increasing porosity, since the presence of air or vacuum in the pores adds insulation. Even though bulk Fe_xN has been successfully fabricated with SPS, porosity was still found due to the high strength of Fe_xN and low sintering temperatures applied. The fraction of porosity in SPSed Fe_xN was decreased with increasing SPS temperature and pressure. Additionally, the density of samples with milled Fe_xN powder is significantly higher than those produced from as-received powder under the same SPS processing conditions.

The sintering temperature is limited by the decomposition temperature of Fe_xN (873 K), so only higher pressures can be used to further decrease sample porosity. Therefore, high density nanostructured Fe_xN components can be developed using high-energy ball-milled Fe_xN powder and novel

SPS double-die setups with SiC plungers. Dense, nanostructured Fe_xN will also have improved thermal conductivity as well as enhanced magnetic properties and mechanical properties. The magnitude of change in electrical conductivity and the thermal conductivity from reduction of porosity requires further investigation. Decreased porosity would also improve magnetic properties, increasing both magnetic saturation and permeability.

Conclusion

In this work, AR micron-sized Fe_xN powder was consolidated using SPS at temperatures of 773 K, 798 K and 823 K, and pressures ranging from 100 to 500 MPa. Nearly fully dense bulk Fe_xN materials were SPSed at 825 K and 350 MPa. SPS with high pressure can be used to consolidate dense Fe_xN at lower temperatures to avoid decomposing of Fe_xN. In addition, three toroids have been directly net shaped using SPS with AR and mechanical milled Fe_xN powder. The high heating efficiency and high pressure of SPS lead to nearly full densification of Fe_xN powder. SPSed Fe_xN shows a high-saturation magnetization of 188 A·m^2/kg. The theoretical value of 209 A·m^2/kg for Fe_4N is within reach through improvements phase purity. Magnetic properties will be improved further through improvements not just in phase purity but also through grain size refinement, and decreased porosity. The sintering behavior and underlying mechanisms that govern Fe_xN consolidation during SPS were discussed in terms of the variation of density as well as the effects of twins in SPSed Fe_xN, in an effort to understand the fundamental phenomena in bulk Fe_xN prepared by SPS processing.

Methods

The starting material used in this study was as-received (AR) commercial Fe_xN powder from Alfa Aesar. The Fe_xN powder exhibits a spherical morphology with particle size of smaller than 45 μm. Bulk Fe_xN samples were consolidated via SPS, using a SPS-825S DR. SINTER (SPS Syntex Inc., Japan) under vacuum conditions (lower than 1 Pa). Generally, pressures up to 100 MPa can be applied with a conventional graphite SPS die, as illustrated in Fig. 8a. In order to apply higher pressures to increase the density of SPSed Fe_xN, a specially designed SPS double-die setup with SiC plungers, as illustrated in Fig. 8b, was utilized.

Figure 9 shows the SEM morphology of (a) AR FexN powder and (b) SPEX mechanical milled (MM) Fe_xN powder. The AR and MM Fe_xN powder were loaded in an assembled die of graphite and SiC. SPS was performed at different temperatures and with a holding time of three minutes. Sintering pressures of 100 to 350 MPa were used for producing disks with a diameter of 10 mm and thickness of 2 mm, as shown in Fig. 9c, and 500 MPa was applied when consolidating disks with a diameter of 5 mm and thickness of 2 mm. Table 1 contains a list of SPSed disk samples and their processing parameters. The purpose of varying sintering temperature and pressure was to investigate their influence on the density, phase transformation, and magnetic behavior of sintered Fe_xN. Three toroids were directly net shaped, eliminating the need for machining, using SPS (798 K and 100 MPa) with AR and milled Fe_xN powder as shown in Fig. 9d. In order to SPS toroidal shaped parts, die were designed according to the desired dimensions of the toroids. A drawing of the SPS graphite die is included in
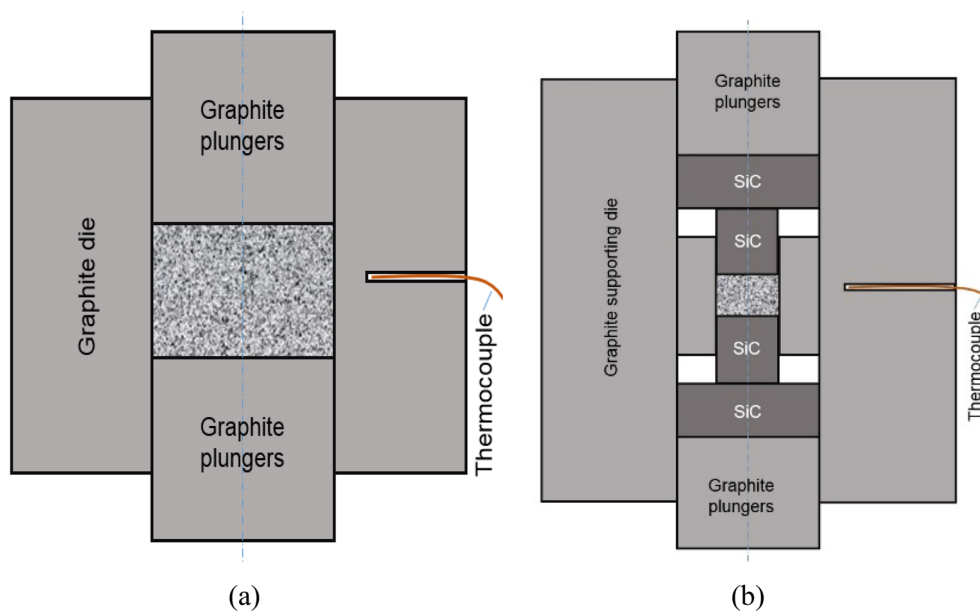

(a)   (b)

Figure 8: Schematic diagram of (a) a conventional graphite SPS die, and (b) a special SPS double-die with SiC plungers.
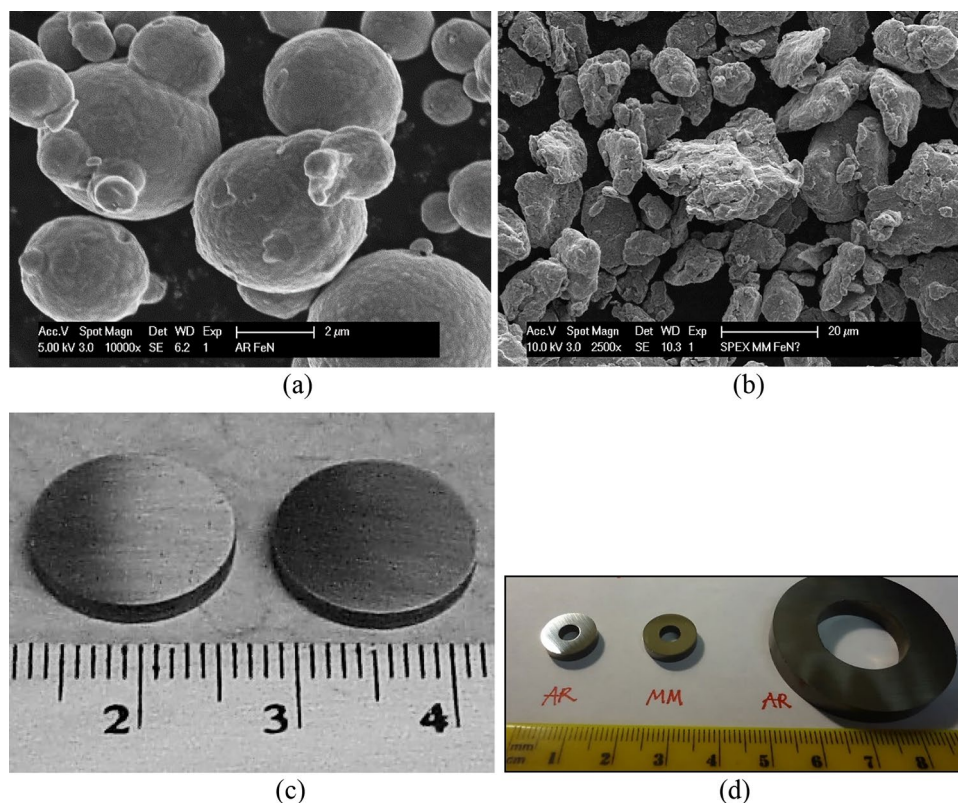
(a)

(b)

(c)

(d)

Figure 9: SEM morphology of (a) AR Fe_xN powder and (b) SPEX milled Fe_xN powder, and pictures of (c) SPSed Fe_xN disks and (d) SPSed net-shaped Fe_xN toroids.

TABLE 1: Process conditions for SPSing Fe_xN powder.

Sample	Powder	Temperature (K)	Pressure (MPa)	Hold time (min)
1	AR Fe_xN powder	773	100	3
2			200	
3			400	
4			500	
5		798	200	
6		823	100	
7			200	
8			350	

the supplementary information (Figure S2). High machining accuracy was required for the graphite dies, especially for the concentric inner and outside diameters of the dies and plungers. Iron nitride powder was added according to the toroid dimensions, filling the space between the outer die and inner mandrel. The sintered toroids are net-shaped, eliminating any need for machining.

The microstructure of SPSed Fe_xN was studied using SEM, energy dispersive X-ray spectroscopy (EDS), and TEM. Additional microstructure information was collected using wavelength dispersive spectroscopy (WDS). WDS analysis was performed on a JEOL JXA-8530F Electron Probe MicroAnalyzer, a Field Emission Microprobe. Beam conditions were a 20 keV, 20 nA, spot beam. Nitrogen Kα was analyzed using an LDE2 crystal with Boron Nitride as the standard. Iron Kα was analyzed using an LIFL crystal with iron metal as the standard. Standards used were on the Taylor Metals Standard Block #2, obtained from Charles M. Taylor.

Thin foils for TEM observations were prepared via mechanical grinding and polishing to a thickness of about 30 μm, followed by ion milling to a thickness of electron transparency using a Gatan precision ion polishing system (PIPS) 691 until perforation occurred. XRD using Cu Kα radiation was utilized for phase identification, and differential scanning calorimetry (DSC) was used for thermal stability studies. The magnetic behavior of the consolidated bulk Fe_xN materials were measured using a Quantum Design MPMS-7 superconducting quantum interference device (SQUID) magnetometer. The density of SPSed Fe_xN samples was measured using an analytical density determination based on the Archimedes principle.

Numerical simulation was also used to elucidate the effect that electrical field has on the formation of interfaces between Fe_xN particles during the SPS process. The governing physics equations are solved numerically using finite element analysis (FEA) as implemented with COMSOL (Palo Alto, CA).

Acknowledgments

Supplementary Information

The online version contains supplementary material available at https://doi.org/10.1557/s43578-021-00379-z.

Open Access

References

1. Y. Li, Y.H. Zhao, W. Liu, Z.H. Zhang, R.G. Vogt, E.J. Lavernia, J.M. Schoenung, Philos. Mag. **90**, 783–792 (2010)
2. S. Bhattacharyya, J. Phys. Chem. C **119**, 1601–1622 (2015)
3. J.M.D. Coey, *Magnetism and Magnetic Materials* (Cambridge University Press, New York, 2010), p. 408
4. A. Fry, Stahl Eisen (in German) **43**, 1271–1279 (1923)
5. K.H. Jack, Proc. R. Soc. A **A208**, 200–215 (1951)
6. T.K. Kim, M. Takahashi, Appl. Phys. Lett. **20**, 492–494 (1972)
7. S. Okamoto, O. Kitakami, Y. Shimada, J. Appl. Phys. **85**, 4952–4954 (1999)
8. A. Leineweber, H. Jacobs, W. Kockelmann, S. Hull, Physica B **276**(278), 266 (2000)
9. A. Tayal, M. Gupta, A. Gupta, V. Ganesan, L. Behera, S. Singh, S. Basu, Surf. Coat. Technol. **275**, 264–269 (2015)
10. Y. Takagi, K. Isami, I. Yamamoto, T. Nakagawa, T. Yokoyama, Phys. Rev. B **81**, 035422 (2010)
11. Z.N. Kayani, S. Riaz, S. Naseem, Surf. Rev. Lett. **21**, 1450013 (2014)
12. P. Prieto, F.J. Palomares, J.M. Gonzalez, R. Pérez-Casero, J.M. Sanz, Surf. Interface Anal. **38**, 392–395 (2006)
13. S. Ito, S. Shinmura, T. Hosokoshi, K. Akashi, J. Jpn. Soc. Powder Metall. **43**, 1415–1419 (1996)
14. H.A. Wriedt, N.A. Gokcen, R.H. Nafziger, Bull. Alloys Phase Diagr. **8**, 355–377 (1987)
15. R. Orrù, R. Licheri, A.M. Locci, A. Cincotti, G. Cao, Mater. Sci. Eng. R. Rep. **63**, 127–287 (2009)
16. S. Lee, H. Kato, T. Kubota, A. Makino, A. Inoue, Intermetallics **17**, 218–221 (2009)
17. N. Zhou, T. Hu, J. Huang, J. Luo, Scr. Mater. **124**, 160–163 (2016)
18. L. Lu, Y.F. Shen, X.H. Chen, L.H. Qian, K. Lu, Science **304**, 422 (2004)
19. B. Zheng, D. Ashford, Y. Zhou, S.N. Mathaudhu, J.-P. Delplanque, E.J. Lavernia, Acta Mater. **61**, 4414–4428 (2013)
20. F.P. Incropera, D.P. DeWitt, *Fundamentals of Heat and Mass Transfer* (Wiley, New York, 1996)
21. Z.A. Munir, U. Anselmi-Tamburini, M. Ohyanagi, J. Mater. Sci. **41**, 763–777 (2006)
22. F.R.N. Nabarro, Scr. Mater. **39**, 1681–1683 (1998)
23. A.J. Haslam, D. Moldovan, V. Yamakov, D. Wolf, S.R. Phillpot, H. Gleiter, Acta Mater. **51**, 2097–2112 (2003)
24. K. Lu, Nat. Rev. Mater. **1**, 16019 (2016)
25. R.M. German, *Sintering Theory and Practice* (Wiley, New York, 1996)
26. G. Herzer, Acta Mater. **61**, 718–734 (2013)
27. Y. Lan, A.J. Minnich, G. Chen, Z. Ren, Adv. Funct. Mater. **20**, 357–376 (2010)
28. M.E. McHenry, M.A. Willard, D.E. Laughlin, Prog. Mater Sci. **44**, 291–433 (1999)